Appl. Phys. B 73, 195–200 (2001)
DOI: 10.1007/s003400100655

Applied Physics B
Lasers and Optics

C. DRAG✉
I. RIBET
M. JEANDRON
M. LEFEBVRE
E. ROSENCHER

Temporal behavior of a high repetition rate infrared optical parametric oscillator based on periodically poled materials

Office National d'Etudes et de Recherches Aérospatiales, B.P. 72, 92322 Châtillon Cedex, France

Received: 23 April 2001
Published online: 19 September 2001 •

ABSTRACT The temporal behavior of a nanosecond pulsed singly resonant periodically poled lithium niobate optical parametric oscillator has been studied both theoretically and experimentally. Taking into account the cylindrical symmetry of the system, a numerical model based on the Hankel transform has been developed. Good agreement is obtained between experiment and simulation. Moreover, the computation time is reduced roughly by a factor of 60 compared to the usual simulation software.

PACS 42.65.Yj; 42.72.Ai

1 Introduction

In the past few years the discovery of new non-linear optical materials, the improvements in the performance of solid-state lasers and progress in high-damage-threshold optics have stimulated renewed interest in optical parametric oscillators (OPOs). Recently, widely tunable low-threshold pulsed (nanosecond) demonstrations of OPOs based on quasi-phase-matched materials such as periodically poled lithium niobate (PPLN) have been numerous in the literature [1–5]. Quasi-phase-matched materials are very attractive because directions of much higher non-linearity become accessible and potentially broader tuning ranges can be obtained.

OPOs based on these new materials display a low threshold and thus allow new compact high repetition rate sources to be used. It has then become timely to investigate in detail the behavior of OPOs according to various physical parameters such as input power, pulse duration, ... Indeed, the high gain of these non-linear materials results in new effects such as strong conversion of signal and idler waves back into the pump waves or 'cascading' effects [6].

These effects influence strongly the efficiency of OPOs. For this reason, some computer simulations and numerical models have been published to interpret laboratory observations and to optimize OPOs' design. Smith and co-workers [7] have constructed a numerical model of a nanosecond seeded OPO taking into account the different interactions in the crystal, non-linear coupling, pump depletion, birefringence, diffraction, walk-off and realistic spatial and temporal beam profiles, with arbitrary cavity-mirror reflectivities and absorption losses in the crystal. The model was used to calculate the performance of a 532-nm-pumped KTP OPO and numerical results were compared with experimental measurements. The calculation program, named SNLO, may be downloaded from the web site of Sandia National Laboratory [8]. In a further publication the same authors describe an OPO with a walk-off-compensating crystal configuration [9] and new methods for modeling a broad-bandwidth, nanosecond OPO in the plane-wave approximation [10]. The spatial properties of the OPO output beam even at high conversion efficiencies, as well as the temporal dynamics of the spatial intensity distribution of OPO pulses, were also studied by Urschel and co-workers [11]. However, all these numerical models are computer-time-consuming and do not allow easy OPO cavity optimization procedures on laboratory computers.

In this paper, we report a numerical model taking into account the cylindrical symmetry of OPOs based on quasi-phase-matched materials, pumped by Gaussian or more generally cylindrical beams. In this case, due to the absence of walk-off, the isotropy of the non-linear crystal allows the use of a one-dimensional Hankel transform rather than a two-dimensional Fourier transform to evaluate spatial frequency components of the different electric fields. The use of cylindrical symmetry enables us to gain a factor of 60 over the calculating time compared to other models. We then compare our model with an experiment carried out with a singly resonant optical parametric oscillator (SROPO) with a 1-cm-long crystal of PPLN. The SROPO is pumped by a high repetition rate YAG laser source emitting at 1.064 μm, in which one can vary independently the pulse duration and the power to study the dynamic behavior of pulses (depleted pump, signal and idler) at the exit of the OPO. The observed dependencies of the output power versus the input pump power are in excellent agreement with these very simple simulations. The experimental data and the numerical model show the importance of the pump depletion, the pump reconstruction and the different behavior between the signal and idler pulses in the dynamics of nanosecond OPOs.

2 Numerical model

The parametric interactions between the pump, signal and idler fields inside the non-linear crystal of the OPOs are classically described by a set of coupled amplitude equa-

✉ Fax: +33-169/93-61-92, E-mail: cyril.drag@onera.fr

tions. We consider here three monochromatic quasi-plane waves propagating along the same direction $\boldsymbol{k}$. In scalar approximation, the total field is given by

$$\boldsymbol{E}(\boldsymbol{r},t)=\sum_{n=1,2,3}\frac{1}{2}\,A_n(\boldsymbol{r},t)\boldsymbol{e}_n\exp\mathrm{i}(\omega_n t-\boldsymbol{k}_n\cdot\boldsymbol{r})+\text{c. c.}, \quad (1)$$

where $\boldsymbol{k}$ is the wavenumber. For periodically poled materials, no walk-off has to be considered in the propagating equations. Also, in the nanosecond regime, the dispersion-velocity differences between optical waves are negligible as well as fast variation of temporal envelope. In the slowly varying approximation and the paraxial approximation and for perfect phase matching, the spatio-temporal variations of the three field amplitudes (A_p, A_s and A_i respectively for the pump, the signal and the idler) are given by [12]

$$\frac{\partial A_\mathrm{s}}{\partial z}=\frac{\mathrm{i}\,\omega_\mathrm{s}}{c\,n_\mathrm{s}}\,d_\mathrm{eff}\,A_\mathrm{i}^*\,A_\mathrm{p}-\frac{\alpha_\mathrm{s}A_\mathrm{s}}{2}-\frac{1}{2\mathrm{i}k_\mathrm{s}}\,\Delta_\perp A_\mathrm{s}, \quad (2)$$

$$\frac{\partial A_\mathrm{i}}{\partial z}=\frac{\mathrm{i}\,\omega_\mathrm{i}}{c\,n_\mathrm{i}}\,d_\mathrm{eff}\,A_\mathrm{s}^*\,A_\mathrm{p}-\frac{\alpha_\mathrm{i}A_\mathrm{i}}{2}-\frac{1}{2\mathrm{i}k_\mathrm{i}}\,\Delta_\perp A_\mathrm{i}, \quad (3)$$

$$\frac{\partial A_\mathrm{p}}{\partial z}=\frac{\mathrm{i}\,\omega_\mathrm{p}}{c\,n_\mathrm{p}}\,d_\mathrm{eff}\,A_\mathrm{s}\,A_\mathrm{i}-\frac{\alpha_\mathrm{p}A_\mathrm{p}}{2}-\frac{1}{2\mathrm{i}k_\mathrm{p}}\,\Delta_\perp A_\mathrm{p}, \quad (4)$$

where d_eff is the effective non-linear coefficient, c the light velocity and α_s, α_i and α_p absorption terms which can be derived from the literature. The symbol $\Delta_\perp$ represents the transverse Laplacian differential operator defined in Cartesian coordinates by

$$\Delta_\perp=\frac{\partial^2}{\partial x^2}+\frac{\partial^2}{\partial y^2}. \quad (5)$$

The first terms on the right-hand sides of (2)–(4) describe the parametric interactions, the second are the absorption losses and the last the diffraction effect. The possibility of back-conversion of signal and idler to pump amplitude is taken into account in (4).

Since these coupled equations (2)–(4) cannot be analytically solved, we develop a numerical model that can be easily run on a laboratory PC (using MatLab software for instance). Although this model can deal with both singly resonant and doubly resonant optical parametric oscillators (SROPO and DROPO), we will only consider here the SROPO case.

The algorithm starts with the spatio-temporal description of the pump field given by our recorded data. The radial dependence is simply given by a Gaussian law:

$$A_\mathrm{p}\simeq A_0\exp\left(-\frac{x^2+y^2}{w_0}\right), \quad (6)$$

where w_0 is the waist of the beam. This planar approximation is still valid providing that the Rayleigh length (z_R) is long compared to the crystal length [12]. On the other hand, the temporal waveform is given by a function $f(t)$ which will be specified in Sect. 3. The incident pump pulse is divided into equal intervals Δt (see Fig. 1a) corresponding to the cavity round-trip time of the signal wave. At each time t, the idler and signal wave amplitudes at the cavity output are calculated by spatially integrating the steady-state parametric equations using the value of the input pump field distribution $A_\mathrm{p}(z=0,r,t)$. The generated signal, idler and depleted pump radiation are transmitted by the output mirror according to the corresponding reflectivity. In the SROPO configuration, only one part of the signal radiation is reflected back at the entrance of the crystal at the time $t+\Delta t$. At this new time, pump, signal and idler waves propagate again using the input pump fields $A_\mathrm{p}(z=0,r,t+\Delta t)$ and $A_\mathrm{s}(z=0,r,t+\Delta t)=r_\mathrm{s}A_\mathrm{s}(z=L,r,t)$, where r_s is the output mirror signal reflectivity (see below for the exact calculation of the return trip in the cavity). The propagation of the three fields is then repeated in the cavity until exhaustion of all the pump temporal samples. For example, the calculations presented in this paper contains 1084 iterations separated by about 0.15 ns. For the first round trip, the amplitudes of the signal and idler fields are given by the vacuum fields (which are equivalent to the intensity of half a photon in the volume of the cavity during the cavity round-trip time) [12].

We now describe the procedure used to calculate the field propagation in the cavity. We use the circular symmetry to form the space grid in the plane perpendicular to the direction of propagation z. The complex fields of the three interacting waves are taken at a fixed number of points along a ray (see Fig. 1b). To avoid numerical problems and to obtain a good resolution of the beam profile, at least 64 points are used for the radial discretization. The spatial step between two points depends on the waist of the pump beam.

spaceskip0.2em plus0.1em minus0.1em The propagation of the beams in the crystal is governed by coupled non-linear differential equations (2)–(4) in the steady-state regime. As can be seen in these equations, the absorption and non-linear coupling terms do not couple with the radial diffraction operator. One thus treats separately the two sets of phenomena: it is the well-known split-step method. Between z and $z+\Delta z$, the system of equations (2)–(4) is integrated using Runge–Kutta algorithms, neglecting the diffraction terms. In the plane $z+\Delta z$, the beams are then diffracted using the radial diffraction operators (cf. (5)). The same operation is then applied to these new fields up to the output of the crystal. The length Δz is optimized during calculation (adaptive step).

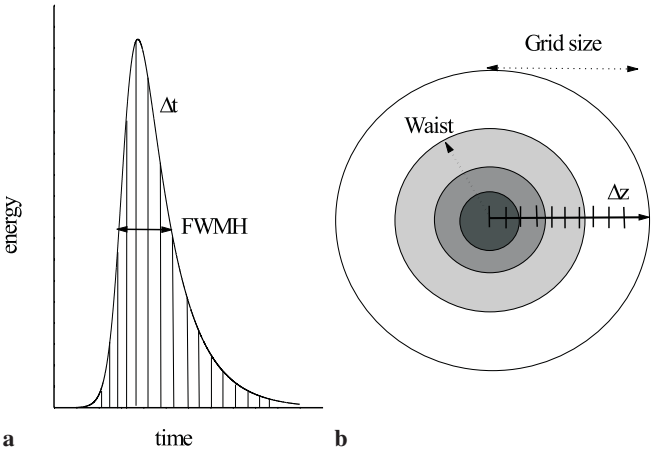

FIGURE 1 Discretization of the pump pulse. **a** Temporal profile divided into equal steps. **b** Gaussian spatial profile and cylindrical calculation grid

As is well known, diffraction operators are conveniently expressed in Fourier space. However, because of the cylindrical symmetry, we have used Hankel transformations instead of Fourier ones, in a way described in detail in the Appendix. These operations are repeated until the waves are propagated from the entrance up to the exit of the non-linear crystal. No parametric interaction is considered during the return trip of the signal wave since quasi-phase-matching is then not effective. On the other hand, the calculation of the return trip takes into account all the parameters of the cavity: diffraction in the vacuum and in the non-linear crystal, reflections on the mirrors (output, input). This whole process is described by the multiplication of the electric field amplitude vector by a square matrix.

The outputs of the calculation are the time variation of the electric-field amplitudes and the phases of the three waves emerging in each point of a transverse plane of the OPO cavity. We can then calculate from these three fields the temporal evolution of powers (J/s) by spatial integration and/or spatial fluences (J/m^2) by temporal integration. For each incident pump power, the calculation takes less than one minute with a Pentium II computer. The same calculation with the SNLO program takes about one hour.

3 Experimental setup

A schematic diagram of our experimental setup is shown in Fig. 2. The mid-infrared beam is produced at the output of the singly resonant OPO pumped with a commercial multimode Q-switched Nd:YAG laser (Light Solutions, model 1010).

For typical operation, the pump laser delivers 500-μJ pulses at 1.064 μm with a 12.5-kHz repetition rate. The laser pulses show an asymmetric temporal shape (see dotted curves in Figs. 4 and 5) with a duration that can be changed between 20 and 45 ns (FWHM), depending on the pumping conditions. These pulses are well fitted in a normalized form by a hyperbolic asymmetric secant:

$$f(t) = \frac{2}{\exp(-t/T_1) + \exp(t/T_2)} \,. \tag{7}$$

A linearly polarized Gaussian beam is available at the output of the Nd:YAG laser with the following specifications: $M^2 = 1.1$ and depolarized ratio < 0.01. A half-wave plate is used in combination with a Glan polarizer to adjust the input energy at the entrance of the OPO. Inside the non-linear crystal, the pump beam radius is reduced to 80 μm ($1/e^2$ of the peak intensity) by means of an antireflection-coated silica lens (150-mm focal length).

The OPO resonator is a stable linear cavity delimited with a pair of dielectric mirrors deposited onto YAG substrates to avoid any residual absorption in the mid-infrared range. The input mirror M1 and the output coupler M2 are spaced 12-mm apart; M1 is flat while M2 is concave with a 50-mm radius of curvature (see Fig. 2). The geometry of the cavity has been designed using an ABCD matrix calculation to ensure a good overlapping of the pump and idler fields within the non-linear crystal. Both mirrors have a high reflectivity ($R > 0.97$) at the signal wavelength (1.65–2.5 μm) and a high transmission ($T > 0.95$) at the pump and idler wavelengths (1.064 and 3.5–4 μm, respectively). In addition, the back side of the two mirrors is antireflection-coated at the three wavelengths and these mirrors can support without optical damage an intensity of 300 MW/cm^2.

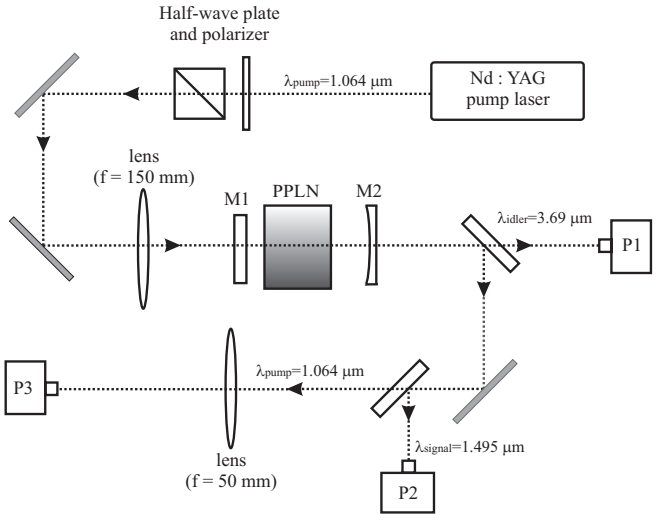

FIGURE 2 Experimental setup. Mirrors M1 and M2 and photodiodes P1, P2 and P3 are described in the text

A multiple-grating PPLN crystal from Crystal Technology Inc. was inserted inside the cavity. This crystal, which is 10-mm long, 10-mm wide and 0.5-mm thick, consists of eight parallel gratings with a spatial period ranging from 28.6 to 29.9 μm. In order to minimize Fresnel losses, the end faces of the PPLN were antireflection-coated at the pump and signal wavelengths. During operation, the PPLN crystal was heated to 140 °C to avoid any photorefractive damage.

The light generated by the OPO is monitored by the use of a variety of instruments. Usually, we employ the 29.7-μm grating period, which quasi-phase matched at 1.495 μm for the signal and at 3.69 μm for the idler. As already mentioned [1, 13], we also observe visible wavelengths at 440.7 nm, 498.8 nm, 532 nm, 622.7 nm and 749.5 nm, which are respectively attributed to non-linear combinations of $\omega_p + 2\omega_s$, $3\omega_s$, $2\omega_p$, $\omega_p + \omega_s$ and $2\omega_s$. At the output of the OPO, a germanium plate (M3 in Fig. 2) is used in combination with a dichroic mirror (M4 in Fig. 2) to separate the idler, signal and pump beams. The time evolution of the different pulses is recorded by means of three photodiodes (P1, P2 and P3 in Fig. 2) connected to a digitizing oscilloscope. Note that a 50-mm-focal-length lens is used to focus the residual pump beam onto the photodiode in order to take account of the total contribution of the beam. Otherwise, a 20-cm-focal-length visible spectrometer (Jobin Yvon) and a broadband power meter are used for measuring the visible wavelengths and the energies of the different output beams.

4 Results and simulations

Figure 3a and b illustrate the dependence of the idler power ($\lambda_i = 3.69$ μm) versus the pump power for two input pulse durations, 21 and 40 ns (FWHM) respectively. In both cases, experimental values were recorded with a 12.5-kHz pumping repetition rate. The parameters of the simulation correspond to the experimental values detailed

above and the refractive indexes ($n(\lambda)$) as well as the second-order non-linear optical coefficient ($d_{\text{eff}} \sim 14$ pm/V) are taken from the literature [14, 15]. Comparison of experimental and calculated values shows a good agreement for the output power versus the input pump power over a large range of operation, whereas the calculated parametric threshold is overestimated by 20%. At low pump power levels, the slope efficiency given in Fig. 3a, b leads to a conversion efficiency ($\eta = P_{\text{i}}/P_{\text{p}}$) of 22%, yielding a total optical conversion efficiency ($\eta' = (P_{\text{i}} + P_{\text{s}})/P_{\text{p}}$) of 73%. This value decreases at high power levels as a consequence of the pump power depletion.

Reducing the pump pulse duration from 40 ns to 21 ns leads to an increase of the experimental threshold intensity from 9.95 MW/cm^2 to 14.4 MW/cm^2. Although the calculated threshold is slightly overestimated, the dependence of the threshold value versus the pump pulse duration is well predicted since the ratio of the calculated thresholds is 1.48 compared to 1.44 for the experiment. Note that the increase of the threshold value at short pump pulse duration is also well described by use of the expression given by Brosnan and Byer [16]. As concerns the slight discrepancy between calculated and measured thresholds, one can argue that all loss terms are not included in our model, such as residual absorption within the coatings and Fresnel reflections on the two faces of the PPLN crystal, especially for the idler field.

Figure 4 illustrates the temporal pulse shapes of the signal and idler fields as well as the input and depleted pump pulses, all responses being normalized to their respective maxima. Experiments have been performed with 21-ns input pulses, for three pump powers leading to different power levels: 1.5, 3 and 5 times above threshold. For each condition, the calculated pulses (see Fig. 4b, d and f) agree well with the experiment (see Fig. 4a, c and e). Whatever the pumping conditions, the signal and idler pulses show an asymmetric shape containing a short rise time followed by a more or less long decrease. Also, from Fig. 4, it is seen that the build-up time of the idler pulse is always shorter than the signal one. Conversely, the signal field persists for a longer time. This temporal behavior illustrates the different dynamics of the signal and idler

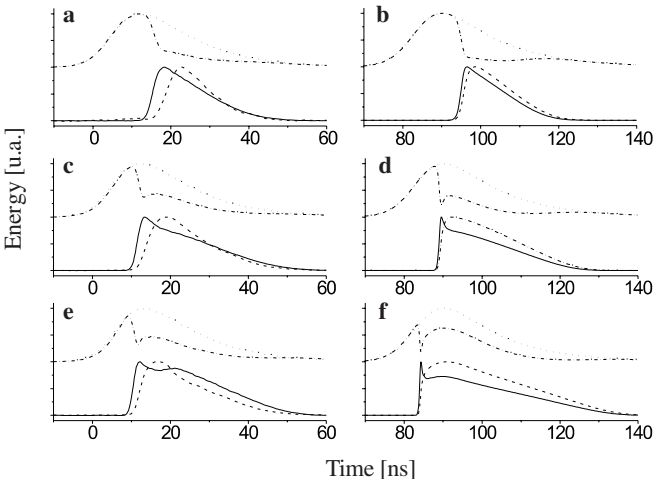

FIGURE 4 Experimental (**a,c** and **e**) and calculated (**b,d** and **f**) pulse shapes. Graphs (**a**) and (**b**) for 1.5 times threshold energy. Graphs (**c**) and (**d**) for three times threshold energy. Graphs (**e**) and (**f**) for five times threshold energy. The *dotted, dot-dashed, solid* and *dashed curves* denote the irradiated pump, the depleted pump, the idler and the signal, respectively

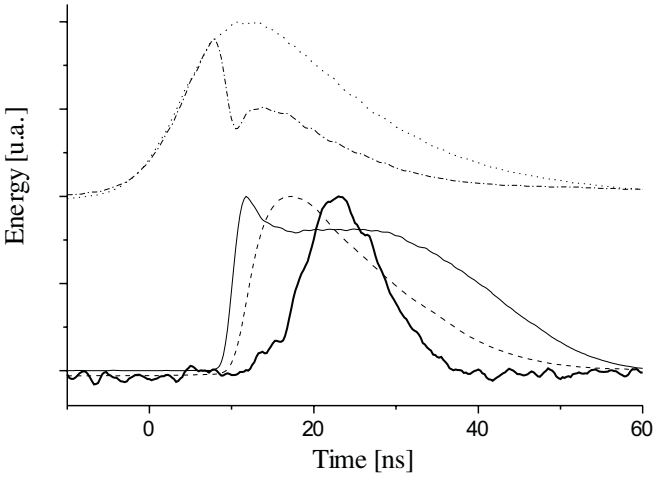

FIGURE 5 'Cascading' effect: experimental pulse shape for four times threshold energy. The *dotted, dot-dashed, solid* and *dashed curves* denote the irradiated pump, the depleted pump, the idler and the signal, respectively. The *bold curve* denotes the idler pulse (at 3.296 μm) of the secondary OPO

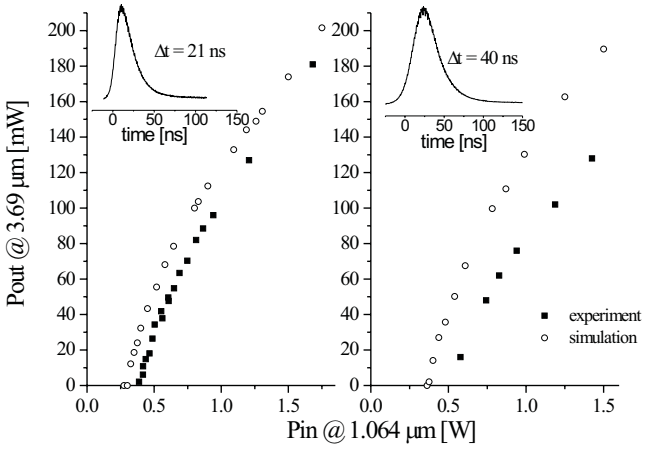

FIGURE 3 Measured (*square*) and calculated (*circle*) output idler power as a function of input pump power. **a** Pulse duration of 21 ns FWHM. **b** Pulse duration of 40 ns FWHM. The *inserts* represent the recorded pump pulses

fields which are coupled in a singly resonant cavity. On the one hand, the non-resonant idler field is produced at the output of the cavity as soon as it is created from the parametric interaction, whereas the signal pulse shows a small delay as a result of the signal energy storage within the cavity. On the other hand, the decay time of the idler field mainly depends on the pumping level, while the damping time of the cavity plays an important role in the signal decrease.

Next, from the temporal responses plotted in Fig. 4, one notices that different operating regimes are accessible with the OPO. Firstly, if the pumping power is fixed at 1.5 times the threshold value (see parts a and b), the signal and idler pulses are detected after the maximum of the pump due to the relatively long build-up time of the fields. Under such conditions, the output pulse clearly shows the pump power depletion as the result of the growth of the signal and idler fields. Secondly, increasing the pump power up to three times the threshold (see parts c and d) reduces the build-up time so

that the signal and idler pulses appear before the maximum of the pump pulse. For this regime, the output pump pulse shows a small overshoot, which is due to a back-conversion process. Thirdly, for the highest pumping value, i.e. five times the threshold value (see parts e and f), one observes that a second maximum appears in the idler pulse. Such a temporal behavior is well described by the model. However, the signal pulse becomes shorter compared to the simulation and the energy of the signal leaves the cavity before the energy of the idler. In fact, this difference is linked to the 'cascading' effect described in [6]. This phenomenon is due to the appearance of a secondary parametric oscillation pumped by the resonant OPO signal itself. Note that the cascading process can take place in our PPLN OPO due to the fortuitous simultaneous phase matching of both OPOs as well as the use of broadband mirrors. As a result of the secondary OPO, the signal energy of the primary OPO shows a small reduction which can be observed during the signal decrease (depletion).

To verify this 'cascading' effect, we have performed a complementary experiment. The existence of the cascading process has been confirmed by analyzing the spectral output of the OPO by means of a mid-infrared spectrometer (model TR25, Jobin Yvon). During this test, the 28.9-μm grating period was used for a crystal temperature of 140 °C, leading to a 1.56-μm signal wavelength and a 3.396-μm idler wavelength. If the pumping power is fixed at a high level, typically four times the threshold value, one observes the production of a 3.296-μm line attributed to the idler field of the cascading OPO. From Fig. 5, it is seen that this new emission appears in coincidence with the primary signal depletion. The wavelength produced at 3.296 μm corresponds to the idler of the secondary OPO and is compatible with the 28.9-μm grating period.

5 Conclusion

A simple numerical model has been described, which takes into account the behavior of a nanosecond pulsed mid-infrared SROPO using isotropic non-linear materials (e.g. PPLN), regarding both the temporal response as well as the input–output characteristics. The model takes advantage of the isotropic nature of the new periodically poled materials (such as PPLN but also PPRTA, PPKTP, ...) by using cylindrical coordinates and describing diffraction in the crystal by a Hankel transform. The agreement between the experiment and the numerical model is excellent in very different situations (pulse duration, pumping level above threshold, ...) in spite of the simplicity of the model. Computation time is typically 60 times shorter than using the usual simulation programs. This model will clearly help in the design of new OPO cavities.

Appendix A: Hankeltransform for the diffraction calculation in parametric interactions

In the slip-step calculation, one needs to compute the diffraction of the different waves $A(x, y, z)$ between z and $z + \mathrm{d}z$ in the non-linear crystal. This is usually done most conveniently in Fourier space. Indeed, the evolution of the two-dimensional (2D) Fourier transform of the diffracted wave $\tilde{A}(\mu, \nu, z + \mathrm{d}z)$ is obtained by a simple product:

$$\tilde{A}(z + \mathrm{d}z) = \tilde{A}(z)\ \exp\left[-\mathrm{i}\pi\frac{\lambda}{n}\left(\mu^2 + \nu^2\right)\mathrm{d}z\right]. \tag{A.1}$$

However, this calculation is time consuming since it involves the 2D Fourier transform of 2D functions $f(x, y)$:

$$\tilde{f}(\mu, \nu) = \frac{1}{2\pi}\int_{-\infty}^{+\infty}\int_{-\infty}^{+\infty} f(x, y)\ \exp[-\mathrm{i}(\mu x + \nu y)]\,\mathrm{d}x\mathrm{d}y. \tag{A.2}$$

This calculation is tremendously simplified if we take the cylindrical symmetry of a function $f(x, y)$ into consideration in the following way. If we introduce the following functions F and $\tilde{F}$ as

$$f(x, y) = f(r\cos\theta, r\sin\theta) = F(r), \tag{A.3}$$

$$\tilde{f}(x, y) = \tilde{f}(\varrho\cos\varphi, \varrho\sin\varphi) = \tilde{F}(\varrho), \tag{A.4}$$

then F and $\tilde{F}$ are related by

$$\tilde{F}(\varrho) = \int_0^{+\infty} J_0(2\pi r\varrho)F(r)r\mathrm{d}r. \tag{A.5}$$

J_0 is the zero-order Bessel function and $\tilde{F}$ is the zero-order Hankel transform of function F. One notes that the integral in (A.5) is one-dimensional while the one in the Cartesian coordinates (A.2) is two-dimensional. Thus calculations of the Hankel transform are far faster than 2D Fourier-transform ones. The wave diffraction between z and $z + \mathrm{d}z$ is described by the differential equation

$$\left(\frac{\partial}{\partial z}A\right)_{\mathrm{diff}} = -\frac{1}{2\mathrm{i}k}\frac{1}{r}\frac{\partial}{\partial r}\left(r\frac{\partial}{\partial r}A\right). \tag{A.6}$$

The Hankel transform of A is then the solution of

$$\left(\frac{\partial}{\partial z}\tilde{A}\right)_{\mathrm{diff}} = -\frac{1}{2\mathrm{i}k}\,\varrho^2\,\tilde{A}, \tag{A.7}$$

which integrates trivially into

$$\tilde{A}(\varrho, z + \mathrm{d}z) = \tilde{A}(\varrho, z)\ \exp\left[-\mathrm{i}\pi\frac{\lambda}{n}\varrho^2\mathrm{d}z\right]. \tag{A.8}$$

Practical implementation of the Hankel transform is quite tricky because the origin $r = 0$ is a singular point. We have used the following numerical procedure to calculate Hankel transforms.

One first notes that the Hankel transform $\tilde{F}$ may be written as

$$\tilde{F}(\varrho) = \tilde{f}(\mu, 0) = \frac{1}{2\pi}\int_{-\infty}^{+\infty}\left[\int_{-\infty}^{+\infty} f(x, y)\,\mathrm{d}y\right]\exp(-\mathrm{i}\mu x)\,\mathrm{d}x, \tag{A.9}$$

so that $\tilde{F}(\varrho)$ is the Fourier transform of

$$p(x) = \int_{-\infty}^{+\infty} f(x, y)\,\mathrm{d}y = \int_{-\infty}^{+\infty} F\left(\sqrt{x^2+y^2}\right)\,\mathrm{d}y. \qquad \text{(A.10)}$$

The procedure is then the following. We first discretize $F(n\Delta r)$ from 0 to $N-1$. We then calculate the intermediate function $p(l\Delta r)$ through (A.10). To obtain good convergence properties of our simulations, we have made use of the following variable-step integration procedure:

$$p(l\Delta r) = 2\Delta r \sum_{n=0}^{n=N-1} \alpha_{l,n}\, F(l\Delta r), \qquad \text{(A.11)}$$

with

$$\alpha_{l,0} = \sqrt{(l+1/2)^2 - l^2}, \qquad \text{(A.12)}$$

$$\alpha_{l,n} = \sqrt{(l+n+1/2)^2 - l^2} - \sqrt{(l+n-1/2)^2 - l^2}. \qquad \text{(A.13)}$$

We thus construct the constant $N \times N$ matrix $\{\alpha_{l,n}\}$ and multiply it by the column vector $\{F(n\Delta r)\}$ to obtain the column vector $\{p(l\Delta r)\}$. The Hankel transform is then obtained by a FFT transform of the column vector $\{p(l\Delta r)\}$. The total procedure is between 50 and 100 times faster than the usual 2D FFT algorithms.

ACKNOWLEDGEMENTS This research is supported by Direction des Programmes pour l'Aviation Civile.

REFERENCES

1 L.E. Myers, R.C. Eckardt, M.M. Fejer, R.L. Byer, W.R. Bosenberg, J.W. Pierce: J. Opt. Soc. Am. B **12**, 2102 (1995)
2 L.E. Myers, W.R. Bosenberg: IEEE J. Quantum Electron. **QE-33**, 1663 (1997)
3 U. Bäder, J.-P. Meyn, J. Bartschke, T. Weber, A. Borsutzky, R. Wallenstein, R.G. Batchko, M.M. Fejer, R.L. Byer: Opt. Lett. **24**, 1608 (1999)
4 M.J. Missey, V. Dominic, P.E. Powers, K.L. Schepler: Opt. Lett. **24**, 1227 (1999)
5 I.F. Elder, J.A.C. Terry: J. Opt. A: Pure Appl. Opt. **2**, L19 (2000)
6 M. Vaidyanathan, R.C. Eckardt, V. Dominic, L.E. Myers, T.P. Grayson: Opt. Express **1**, 49 (1997)
7 A.V. Smith, W.J. Alford, T.D. Raymond, M.S. Bowers: J. Opt. Soc. Am. B **12**, 2253 (1995)
8 http://www.sandia.gov/imrl/XWEB1128/xxtal.htm
9 D.J. Armstrong, W.J. Alford, T.D. Raymond, A.V. Smith, M.S. Bowers: J. Opt. Soc. Am. B **14**, 460 (1997)
10 A.V. Smith, R.J. Gehr, M.S. Bowers: J. Opt. Soc. Am. B **16**, 609 (1999)
11 R. Urschel, A. Borsutzky, R. Wallenstein: Appl. Phys. B **70**, 203 (2000)
12 A. Yariv: *Quantum Electronics* (Wiley, New York 1989)
13 P. Schulp, S.D. Butterworth, I.T. McKinnie: Opt. Commun. **154**, 191 (1998)
14 D.H. Jundt: Opt. Lett. **22**, 1553 (1997)
15 I. Shoji, T. Kondo, A. Kitamoto, M. Shirane, R. Ito: J. Opt. Soc. Am. B **14**, 2268 (1997)
16 S.J. Brosnan, R.L. Byer: IEEE J. Quantum Electron. **QE-15**, 415 (1979)